Wideband High-Efficiency Six-Beam Full-Metal Satellite L-Band Antenna Array

Javier Vera-Sánchez, Miguel Ferrando-Rocher, Gorka Casasus-Goyeneche, and Miguel Ferrando-Bataller
Antennas and Propagation Lab of Universitat Politècnica de València, Spain
jversan2@upv.es

***Abstract*—This paper presents a high-efficiency multi-beam L-band antenna with a simple feeding approach, targeting a cost-effective, low-profile, lightweight, and robust solution suitable for integration on board a LEO satellite. The antenna concept provides six distinct beams, enabling full 360° azimuth coverage while maintaining a mechanically simple overall architecture. The work is carried out within the SATERA project, funded under the Horizon Europe framework programme, which aims to advance aerial surveillance through satellite-based technologies and to address coverage limitations in remote and oceanic regions. As a proof of concept for spaceborne and airborne reception of aeronautical surveillance signals, including Automatic Dependent Surveillance–Broadcast (ADS-B) reception, a preliminary six-beam design is introduced and its key performance parameters are evaluated as a baseline for further development. The early results support the feasibility of the proposed approach and its potential integration into the broader SATERA system, as well as multi-service L-band reception.**

I. Introduction

The rapid growth of aeronautical surveillance, satellite-based navigation, and non-terrestrial networks (NTN) has created strong demand for compact, broadband L-band antennas capable of supporting multiple services within a single aperture. While ADS-B and Mode-S at 1090 MHz remain the dominant civil aviation links, modern airborne and spaceborne platforms increasingly require simultaneous access to GNSS (L2/L5), DME/TACAN, telemetry, and spectrum-monitoring services across 1–1.4 GHz [1], [2]. Under stringent constraints on mass, volume, power, and reliability, there is growing interest in antenna architectures that provide broad impedance bandwidth, controlled radiation patterns, and mechanical simplicity, enabling replacement of multiple narrowband radiators by a single multifunctional antenna.

Most current ADS-B and aeronautical navigation antennas are based on quarter-wave monopoles and blade antennas installed on aircraft fuselages, low-profile patch and array antennas embarked on satellites and similar monopole or patch-based installations at ground stations [3]–[8]. Although robust and well understood, they are typically narrowband and poorly suited for simultaneous reception of GNSS L2/L5 or higher-frequency L-band channels, often forcing the use of multiple dedicated antennas that increase drag, installation complexity, and failure probability. Satellite ADS-B payloads and spaceborne receivers commonly employ patch arrays or cavity-backed radiators to achieve hemispherical coverage and polarization purity [9], [10], but these are often narrowband, mechanically bulky, or costly, and offer limited flexibility for true multi-service operation. Moreover, conventional patch-based solutions tend to favor zenith-pointing reception, providing restricted low-elevation coverage, which is critical for long-range ADS-B and NTN-type links. Electrically large arrays can improve directivity but at the expense of mass, feed complexity, and robustness [11].

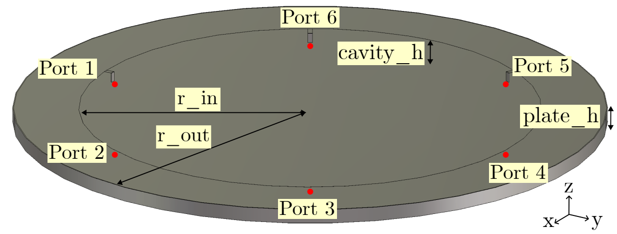

Fig. 1: General view of the annular metallic cavity antenna, with ports and dimensions highlighted.

These limitations highlight the lack of a compact, low-profile, electrically broadband L-band antenna that can support multiple aeronautical and spaceborne services with a single, mechanically simple aperture while still providing suitable radiation characteristics for long-range surveillance and navigation. This paper addresses this gap by proposing a ring-shaped broadband L-band antenna, illustrated in Fig. 1, which consists of an annular metallic cavity loaded with multiple inverted-L-type (ILA) monopoles. Each ILA element is capacitively loaded to achieve broadband impedance behavior, while the surrounding ring cavity is used to support higher-order modes and shape the composite pattern. The resulting “paella-like” circular aperture provides approximately 360° azimuth coverage with an elevation pattern tailored to favor low-to-medium elevation angles, suitable for long-range ADS-B and NTN-type links.

Compared with conventional patch arrays or blade antennas, the proposed architecture offers: (i) broadband impedance matching that spans multiple L-band services around the 1090 MHz ADS-B center frequency; (ii) multi-service capability within a single compact aperture; (iii) a simple, failure-tolerant array topology, since multiple ILA elements contribute to the overall pattern; and (iv) potential for low-cost, lightweight, and mechanically robust implementations compatible with aeronautical and spaceborne environments. The remainder of this paper is organized as follows. Section II describes the antenna architecture and ring-cavity ILA concept. Section III presents simulated impedance and radiation results. Section IV concludes the paper and outlines future developments.

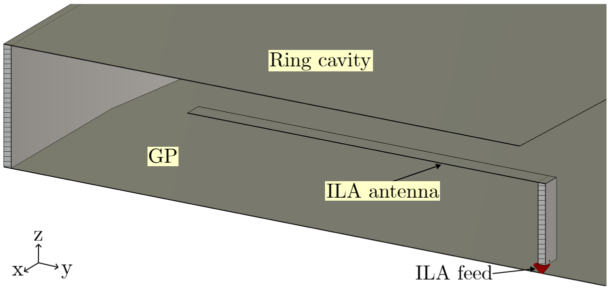

Fig. 2: Close-up view of one of the six ILA radiators, highlighting its main parts and dimensions.

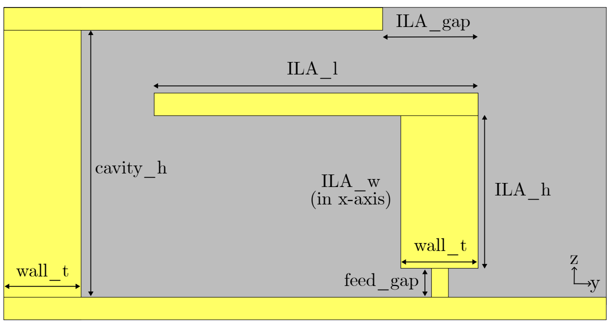

Fig. 3: Further detailed schematic of the ILA radiator, showing the remaining dimensions.

TABLE I: Geometrical design parameters of the ILA radiators and the annular metallic cavity.

Design parameter	**Specified value**
Ring cavity geometry	
Outer ring radius, r_out	309.6 mm
Inner ring radius, r_in	240.8 mm
Ring plate height, $plate\_h$	15.07 mm
ILA antenna geometry	
Top horizontal strip length, ILA_l	47.58 mm
Vertical strip height, ILA_h	10 mm
Strip width, ILA_w	5 mm
Other parameters	
Horizontal gap between ILA and ring, ILA_gap	3.07 mm
Feeding gap between ILA and GP, $feed\_gap$	1 mm
Cavity height, $cavity\_h$	15 mm
Metal wall thickness, $wall\_t$	1 mm

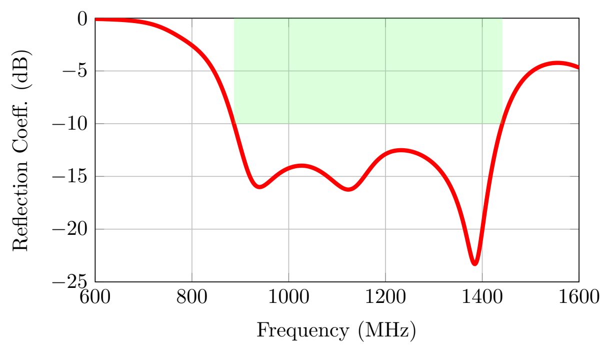

Fig. 4: Simulated reflection coefficient S_{11} of one ILA radiator.

II. Antenna Description

The proposed antenna consists of a six-element inverted-L antenna (ILA) array embedded in a circular annular metallic cavity. A detailed view of the ILA antenna and the cavity is presented in Fig. 2. Each capacitively loaded ILA provides a low-profile broadband radiator, while the cavity controls the array impedance and radiation pattern.

Each ILA element comprises a short vertical arm of $10\,\mathrm{mm}$ height connected to the feed and a horizontal arm of $47.58\,\mathrm{mm}$ by $5\,\mathrm{mm}$ extending radially. This top-loaded geometry increases the effective electrical length and lowers the fundamental resonance so that efficient radiation is obtained despite the strongly constrained height. A $1\,\mathrm{mm}$ gap between the lower part of the ILA and the ground plane introduces an additional, tunable capacitive coupling that is used to finely adjust the input reactance and stabilize the impedance response over the L-band. The main geometric parameters of the cavity and ILA are listed in Table I, and Fig. 3 shows the detailed geometry of the ILA and its placement inside the cavity.

The six ILA elements are placed inside a $15\,\mathrm{mm}$-high, air-filled annular cavity that surrounds them in a ring configuration. The upper rim of the cavity is located close to the ILA horizontal arms, providing extra capacitive coupling between the element tips and the cavity wall. This interaction further increases the effective electrical length of each radiator and introduces controlled reactive loading that broadens the impedance bandwidth and stabilizes the resonances. The cavity rim acts as a nearby conducting boundary that reshapes the near field, improving matching and promoting multi-mode operation across the band.

Beyond impedance control, the annular cavity also acts as a reflector that shapes the far-field pattern. Currents induced on the cavity walls generate image sources that steer the main beam away from zenith toward mid-elevation angles, yielding a primary lobe around $45°$–$50°$ above the horizon. This elevation tilt, combined with the ring arrangement of six ILAs, enables broadband operation with controlled radiation characteristics, mid-elevation coverage, and high radiation efficiency within a compact, mechanically simple structure.

III. Simulated Results

The simulated reflection coefficient of a single ILA element is shown in Fig. 4. The antenna exhibits a very wide impedance bandwidth of approximately 550 MHz, with three dominant resonances located near 950 MHz, 1130 MHz and 1400 MHz. This multi-resonant behavior provides continuous coverage across a large portion of the L-band, making the proposed radiator suitable for multiple aeronautical and spaceborne services, including ADS-B, GNSS, and navigation aids.

The corresponding input impedance is shown in Fig. 5 in terms of its real and imaginary components. Over the main operating band highlighted in Fig. 5, the real part remains centered around 50 Ω, indicating efficient power transfer to the radiator over a wide frequency range. Several impedance

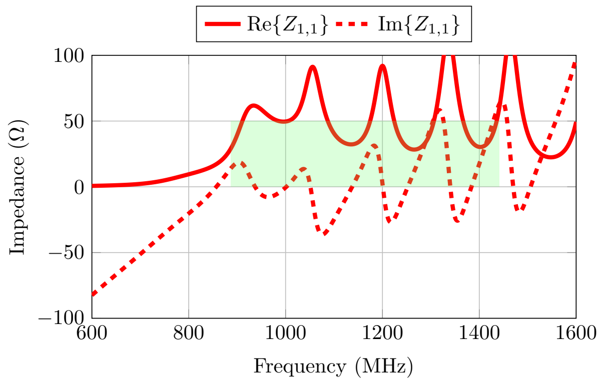

Fig. 5: Simulated input impedance Z_{11} of port one.

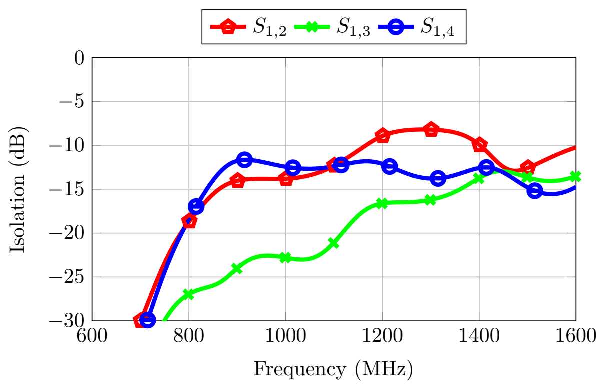

Fig. 6: Simulated Isolation of port one.

peaks are observed, associated with the multiple resonant modes of the capacitively loaded ILA and its interaction with the surrounding cavity; however, these peaks do not significantly degrade the impedance matching within the targeted L-band. Importantly, the imaginary part oscillates around 0 Ω throughout the band, showing that the antenna remains close to resonance across multiple frequencies and that the reactive component of the input impedance is effectively compensated. This multi-resonant but well-balanced impedance behavior explains the broadband $|S_{11}|$ response and supports multi-service operation across the L-band.

Mutual coupling between the six ILA elements is illustrated in Fig. 6. The curves $|S_{13}|$ and $|S_{14}|$ correspond to the element next-to-nearest to port 1 and the element located diametrically opposite in the ring, respectively. These couplings are slightly exceeding the -15 dB guideline but do not significantly affect the overall radiation performance due to the increased physical separation and weak field overlap. The red curve represents adjacent-element coupling (e.g., $|S_{12}|$), which increases above -10 dB beyond approximately 1.2 GHz. In future design iterations, this behavior will be mitigated through the introduction of shorting elements or similar decoupling techniques. Owing to the geometric symmetry of the structure, $|S_{15}|$ and $|S_{16}|$ are identical to $|S_{13}|$ and $|S_{14}|$, respectively, and are therefore omitted from the figure.

The elevation radiation characteristics of a single excited

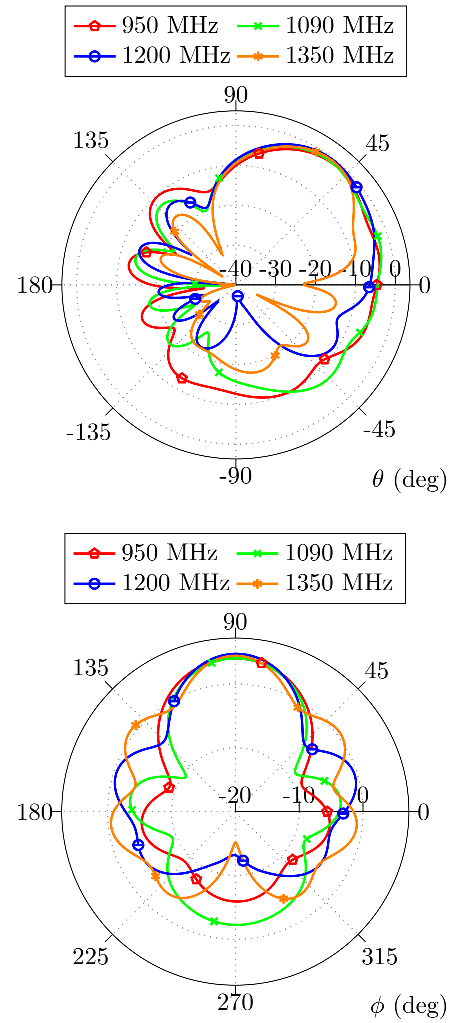

Fig. 7: Simulated normalized radiation patterns at 4 different frequencies of the antenna in the following cuts: (above) $\phi = 90°$ and (below) $\theta = 50°$.

port are shown in Fig. 7 (above) for $\phi = 90°$ at 950, 1090, 1200, and 1300 MHz. In all cases, the maximum radiation occurs around $\theta \approx 50°$, confirming that the annular cavity effectively tilts the main beam toward a mid-elevation angle suitable for long-range aeronautical and NTN-type links. As summarized in Table II, the directivity remains above 10 dBi, and the lower frequencies exhibit efficiencies exceeding 80%. The directivity increases slightly with frequency, while the main-lobe beamwidth in elevation decreases from about 70° at the lower frequencies to approximately 40° at the upper end of the band. This broad elevation coverage enables the antenna to illuminate a large angular sector extending from the direction of maximum radiation toward the horizon and down toward the nadir, without requiring electronic or mechanical beam steering.

The corresponding azimuth cuts presented in Fig. 7 (below) show that the individual beams maintain similar directivity

TABLE II: Directivity, realized gain, and efficiency of the proposed antenna.

f (MHz)	D (dBi)	G_r (dBi)	η (%)
950	10.00	9.20	83
1130	10.01	9.10	76
1400	10.41	8.19	60

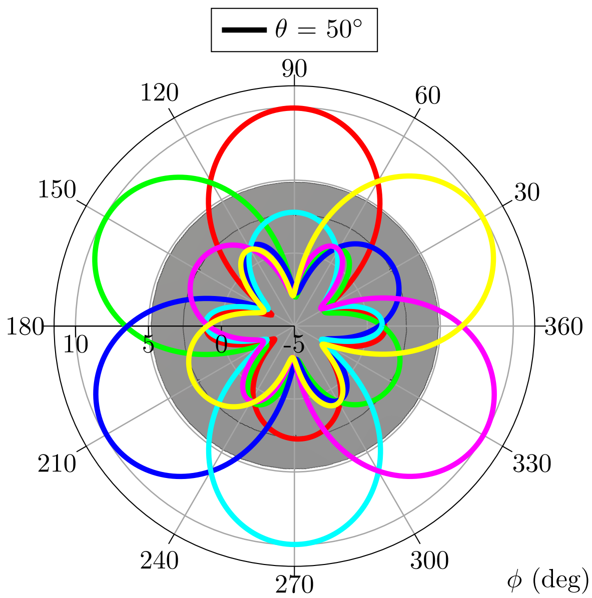

Fig. 8: Radiation-pattern cut at $\theta = 50°$ at 1000 MHz for the six-port antenna, demonstrating the simultaneous reception of all six beams.

and beamwidth over most of the operating band. Only at the highest frequency, around 1.35 GHz, does the azimuthal beamwidth reduce to approximately $40°$, which remains sufficient to ensure complete coverage when the six beams are combined. Fig. 8 further illustrates the azimuth cut at $\theta = 50°$ and 950 MHz, where the six beams collectively provide effective $360°$ coverage. A top view of the antenna included in the figure indicates the relative positions of the feeding ports and the associated beam directions, confirming that the proposed six-element ring configuration achieves uniform azimuthal coverage at the desired elevation angle.

Overall, the simulated results demonstrate that the proposed ring-cavity ILA array combines wide impedance bandwidth, manageable inter-element coupling, a controlled elevation tilt around $50°$, and full $360°$ azimuthal coverage using only six radiating elements, thereby meeting the key requirements for broadband L-band aeronautical and spaceborne reception.

IV. Conclusions

This paper has presented a compact broadband L-band antenna based on a six-element inverted-L array embedded in an annular metallic cavity. The combination of electrically short, capacitively loaded ILAs with a low-profile air-filled cavity and full-metal structure yields wide impedance bandwidth, controlled radiation characteristics, and a mechanically simple structure suitable for aeronautical and spaceborne platforms. Simulation results confirm three resonances around 950 MHz, 1130 MHz, and 1400 MHz, stable matching, directivity over 10 dBi, manageable coupling, and a radiation pattern with an elevation maximum near $\theta \approx 50°$ and effective $360°$ azimuth coverage. The antenna is therefore a promising candidate for multi-service reception, including ADS-B/Mode-S, GNSS L2/L5, DME/TACAN, and L-band satellite applications, with future work focused on further coupling reduction, mechanical ruggedization, and experimental validation.

Acknowledgment

This research was conducted within the SATERA project, which has received funding from the SESAR 3 Joint Undertaking (JU) under grant agreement No. 101164313, with support from the European Union's Horizon Europe research and innovation programme and the SESAR 3 JU members other than the Union. Additional support was provided by Spain's Ministerio de Ciencia e Innovación under research projects PID2022-136869NB-C33 and PID2022-141055NB-C21.

References

[1] D. Gómez Depoorter and W. Kellerer, "Designing the air–ground data links for future air traffic control communications," *IEEE Transactions on Aerospace and Electronic Systems*, vol. 55, no. 1, pp. 135–146, 2019.

[2] R. Onrubia, J. Querol, D. Pascual, A. Alonso-Arroyo, H. Park, and A. Camps, "DME/TACAN Impact Analysis on GNSS Reflectometry," *IEEE Journal of Selected Topics in Applied Earth Observations and Remote Sensing*, vol. 9, no. 10, pp. 4611–4620, 2016.

[3] J. Budroweit and M. Drobczyk, "Design of a Small Size, Low Profile L-Band Antenna, Optimized for Space-Based ADS-B Signal Reception," in *2018 International Conference on Radar (RADAR)*, 2018, pp. 1–6.

[4] G. Priscila, L. O. Nur, and Edwar, "A Design of ADS-B Receiver Antenna using Truncated Circular Microstrip Patch in Cubesat Form Factor," in *2022 IEEE International Conference on Aerospace Electronics and Remote Sensing Technology (ICARES)*, 2022, pp. 1–6.

[5] Y. Luo, W. Wang, L. Sang, Y. Sun, X. Wang, G. Xu, Q. Zeng, and S. S. Gao, "All-metal broadband low-profile dual-frequency dual circularly polarized aperture-shared antenna for spaceborne applications," *IEEE Antennas and Wireless Propagation Letters*, vol. 24, no. 7, pp. 1819–1823, 2025.

[6] Z. Hamouda, S. Azaizia, A. Bouziane, Z. Mordi, and T. Lasri, "Development of a miniaturized broadband blade antenna for aeronautical applications," in *2023 17th European Conference on Antennas and Propagation (EuCAP)*, 2023, pp. 1–5.

[7] Y. Sun and C. Mao, "A low-cost low-profile dual-band dual-circularly polarized antenna with shared-radiator for l-/s-band phased array applications," *IEEE Transactions on Antennas and Propagation*, pp. 1–1, 2025.

[8] Y.-Q. Wen, B.-Z. Wang, and X. Ding, "Wide-beam circularly polarized microstrip magnetic-electric dipole antenna for wide-angle scanning phased array," *IEEE Antennas and Wireless Propagation Letters*, vol. 16, pp. 428–431, 2017.

[9] J. Vera-Sánchez, M. Ferrando-Rocher, G. Casasus-Goyeneche, and M. Ferrando-Bataller, "L-Band Unit-Cell Antenna Design for Satellite-Based ADS-B Surveillance," in *2025 IEEE International Symposium on Antennas and Propagation and North American Radio Science Meeting (AP-S/CNC-USNC-URSI)*, 2025, pp. 1893–1895.

[10] J. Vera-Sánchez, Martín-Nüñez, M. Ferrando-Rocher, and M. Ferrando-Bataller, "Circularly Polarized Conical Array for ADS-B Applications in LEO Satellites," in *2025 19th European Conference on Antennas and Propagation (EuCAP)*, 2025, pp. 1–3.

[11] M. Sureda, M. Sobrino, O. Millan, A. Aguilella, A. Solanellas, M. Badia, J. F. Munoz-Martin, L. Fernandez, J. A. Ruiz-De-Azua, and A. Camps, "Design and testing of a helix antenna deployment system for a 1u cubesat," *IEEE Access*, vol. 9, pp. 66 103–66 114, 2021.